*J. Fluid Mech.* (2009), *vol.* 618, *pp.* 323–348. © 2008 Cambridge University Press 
doi:10.1017/S0022112008004242 Printed in the United Kingdom

# Convective/absolute instability in miscible core-annular flow. Part 2. Numerical simulations and nonlinear global modes

B. SELVAM[1], L. TALON[2], L. LESSHAFFT[1] AND E. MEIBURG[1]†

[1]Department of Mechanical Engineering, University of California, Santa Barbara, CA 93106, USA

[2]FAST, Universités Paris *VI* et Paris *XI*, CNRS (UMR 7608) Bâtiment 502, Campus Universitaire, 91405 Orsay Cedex, France

(Received 6 December 2007 and in revised form 15 September 2008)

The convective/absolute nature of the instability of miscible core-annular flow with variable viscosity is investigated via linear stability analysis and nonlinear simulations. From linear analysis, it is found that miscible core-annular flows with the more viscous fluid in the core are at most convectively unstable. On the other hand, flows with the less viscous fluid in the core exhibit absolute instability at high viscosity ratios, over a limited range of core radii. Nonlinear direct numerical simulations in a semi-infinite domain display self-excited intrinsic oscillations if and only if the underlying base flow exhibits absolute instability. This oscillator-type flow behaviour is demonstrated to be associated with the presence of a nonlinear global mode. Both the parameter range of global instability and the intrinsically selected frequency of nonlinear oscillations, as observed in the simulation, are accurately predicted from linear criteria. In convectively unstable situations, the flow is shown to respond to external forcing over an unstable range of frequencies, in quantitative agreement with linear theory. As discussed in part 1 of this study (d'Olce, Martin, Rakotomalala, Salin and Talon, *J. Fluid Mech.*, vol. 618, 2008, pp. 305–322), self-excited synchronized oscillations were also observed experimentally. An interpretation of these experiments is attempted on the basis of the numerical results presented here.

## 1. Introduction

The stability of core-annular flow, the concentric flow of two different fluids in a pipe, was first investigated by Hickox (1971). Motivated by the application of lubricated pipelining, Chen, Bai & Joseph (1990) and Bai, Chen & Joseph (1992) experimentally studied the effect of viscosity and density differences on the dynamics of core-annular flow composed of two immiscible fluids. The stability of such immiscible configurations has further been investigated by means of linear stability analysis (Joseph, Renardy & Renardy 1984; Hu & Joseph 1989; Preziosi, Chen & Joseph 1989; Hu, Lundgren & Joseph 1990; Boomkamp & Miesen 1992; Hu & Patankar 1995) as well as nonlinear numerical simulation (Li & Renardy 1999; Kouris & Tsamopoulos 2001, 2002). Several unstable flow regimes have been identified, depending on the viscosity ratio, flow rate and volume fraction of the two fluids (see the review by Joseph *et al.* 1997). The case of miscible core-annular flows

† Email address for correspondence: meiburg@engineering.ucsb.edu

https://doi.org/10.1017/S0022112008004242 Published online by Cambridge University Press

has received less attention to this day. Several authors have addressed miscible variable viscosity displacements in capillary tubes, both experimentally and numerically (Chen & Meiburg 1996; Petitjeans & Maxworthy 1996; Scoffoni, Lajeunesse & Homsy 2001; Kuang, Maxworthy & Petitjeans 2003; Balasubramaniam *et al.* 2005). These investigations focused on front propagation velocities, and on the fraction of the more viscous fluid left behind on the wall. In a recent study, Selvam *et al.* (2007) explored the temporal linear stability properties of miscible core-annular flow. It was found that these flows may sustain both axisymmetric and helical instability modes, the axisymmetric mode being dominant at high Schmidt numbers.

However, it may be expected that low-level disturbances in an experimental setting primarily originate from the upstream injector apparatus, and subsequently experience unstable growth as they propagate down the tube. In the context of linear stability theory, such a situation is best described in a spatial, rather than temporal framework. The spatial stability properties of miscible core-annular flows are investigated in the present paper.

The companion article by d'Olce *et al.* (2009) (referred to as 'part 1' hereafter) presents results of an experimental study of miscible core-annular flows in which a more viscous annular fluid surrounds a less viscous core fluid. The most striking observation from these experiments is the occurrence of synchronized oscillations, in the form of regular vortical structures, which seem to arise naturally in the absence of explicit forcing. The findings suggest that these oscillations may be self-sustained, i.e. that they are the result of intrinsic flow dynamics, rather than a response to external perturbations. Flows that undergo spontaneous transition from a steady state to a state of intrinsic oscillations are said to be globally unstable (see Huerre & Monkewitz 1990). It has been demonstrated for several flow configurations that global instability is closely connected to the presence of local absolute instability in a region of the unperturbed flow state. A brief review of such flows is given in Chomaz (2005). In the experiments of part 1, practical limitations make it difficult to precisely demarcate the global instability regime. Hence, the present paper aims to complement the experimental results, and to provide the information that is required for an interpretation in terms of nonlinear global mode theory.

The main objective of this study is to characterize for the first time the nonlinear global instability of miscible core-annular flow. In a system with an upstream boundary such as a nozzle, the base flow is non-parallel. As opposed to strictly local linear theory, nonlinear global stability concepts become necessary to describe the spatio-temporal dynamics of such flows. Nonetheless, these nonlinear global properties may be deduced from a linear local analysis under certain conditions, mainly the assumption that non-parallel base flow variations are slow compared to the instability wavelength (Chomaz, Huerre & Redekopp 1991; Monkewitz, Huerre & Chomaz 1993). An extensive theoretical framework for global modes and their connection with linear absolute instability has been developed in the context of Ginzburg–Landau models under both parallel and non-parallel conditions (Chomaz, Huerre & Redekopp 1988; Couairon & Chomaz 1997*a*, *b*, 1999; Pier, Huerre & Chomaz 2001). In the case of a semi-infinite domain with a Dirichlet upstream boundary, Couairon & Chomaz (1997 *b*) have shown that self-sustained oscillations may occur via a Hopf bifurcation, under the condition that a sufficiently large region of local absolute instability exists near the upstream boundary. Furthermore, Couairon & Chomaz (1997 *b*) demonstrated via asymptotic matching that, at the global instability threshold, the global frequency is equal to the linear absolute frequency at the inlet. Couairon & Chomaz (1999) further derived explicit scaling laws

https://doi.org/10.1017/S0022112008004242 Published online by Cambridge University Press

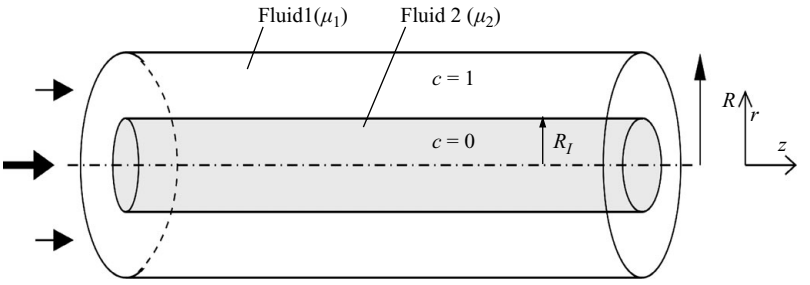



FIGURE 1. Principal sketch of a core-annular flow of two miscible fluids of different viscosities and equal densities in a capillary tube of radius $R$. Fluid 2 of viscosity $\mu_2$ occupies the core with a radius $R_I$, encapsulated by the fluid 1 of viscosity $\mu_1$.

for the amplitude of nonlinear global modes, all in the context of Ginzburg–Landau model equations. These model predictions have been found to hold true in several real flows, such as wakes (Chomaz 2003) and hot jets (Lesshafft, Huerre & Sagaut 2007).

The paper is organized as follows. The physical problem is formulated in § 2. The governing equations and dimensionless parameters are stated here. In § 3, the formalism of the linear stability analysis is laid out and results are discussed, with a focus on the convective/absolute transition. Section 4 describes the numerical implementation of the nonlinear simulations and presents the results with a focus on the global instability of miscible core-annular flows. Section 5 compares the numerical results to those of the experiments in part 1. The main findings of the present work are summarized in § 6.

## 2. Problem formulation

Consider an axisymmetric pipe of radius $R$ into which two miscible fluids are injected at the upstream end to form two concentrically flowing streams (see figure 1). The radial location of the interface ($R_I$) between these two fluids is determined by the volume fractions of the two injected fluids. Since the two fluids are miscible, the transition zone in the concentration profile exhibits a finite thickness (herein referred to as interface thickness), due to the effects of diffusion. Fluid 1 forms a film of constant thickness along the wall of the tube, while fluid 2 occupies the centre of the tube (cf. figure 1). The two fluids are assumed to be of equal densities ($\rho_1 = \rho_2$) but different viscosities $\mu_1$ and $\mu_2$. The axial and radial coordinates are denoted by $z$ and $r$, respectively.

### 2.1. *Governing equations*

We employ the incompressible Navier–Stokes equations, along with a convection–diffusion equation for species conservation

$$\nabla \cdot \boldsymbol{v} = 0, \tag{2.1}$$

$$\rho\left(\frac{\partial \boldsymbol{v}}{\partial t} + \boldsymbol{v} \cdot \nabla \boldsymbol{v}\right) = -\nabla p + \nabla \cdot \boldsymbol{\tau}, \tag{2.2}$$

$$\delta t c + \boldsymbol{v} \cdot \nabla c = D \nabla^2 c, \tag{2.3}$$

where $\boldsymbol{v} = (v_r, v_\theta, v_z)$ denotes the flow velocity, $\tau = \mu\left(\nabla \boldsymbol{v} + \nabla \boldsymbol{v}^T\right)$ the viscous stress tensor and $c$ the concentration normalized by that of the outer fluid. The elements of the viscous stress tensor $\tau_{ij}$ are defined in the usual way in cylindrical coordinates (Panton 1984). The diffusion coefficient $D$ is assumed constant throughout the mixture. In specifying a constitutive relation between viscosity and concentration, we follow

https://doi.org/10.1017/S0022112008004242 Published online by Cambridge University Press

earlier works in literature (Tan & Homsy 1986; Goyal & Meiburg 2006) and assume the viscosity $\mu$ to be an exponential function of the concentration

$$\mu = \mu_2 \mathrm{e}^{Mc}, \quad M = \ln \frac{\mu_1}{\mu_2}. \tag{2.4}$$

Note that by definition, positive $M$ corresponds to less viscous fluid in the core and more viscous fluid in the annular region. To be consistent, the above governing equations are non-dimensionalized with the same characteristic scales as in part 1. Hence, we choose the radius of the outer tube ($R$) as characteristic length $L^*$ and the viscosity of the inner fluid ($\mu_2$) as the characteristic viscosity $\mu^*$. The velocity averaged over the cross-section is employed as the characteristic velocity $V^*$

$$V^* = \frac{|\,\dot{Q}\,|}{\pi R^2},$$

where $\dot{Q}$ denotes the volumetric flow rate. Then the characteristic time and pressure are defined as

$$t^* = \frac{L^*}{V^*} \qquad \text{and} \qquad P^* = \frac{\mu^* V^*}{L^*}.$$

Since the experimentally observed instabilities in part 1 are axisymmetric, we assume symmetry about the centreline of the tube, thus avoiding the singularity associated with the axis for our later nonlinear simulations. We thus obtain the axisymmetric governing dimensionless equations of the form

$$\frac{\partial v_r}{\partial r} + \frac{v_r}{r} + \frac{\partial v_z}{\partial z} = 0, \tag{2.5}$$

$$Re\left[\frac{\partial v_r}{\partial t} + v_r\frac{\partial v_r}{\partial r} + v_z\frac{\partial v_r}{\partial z}\right] = -\frac{\partial p}{\partial r} + e^{Mc}\left[\frac{\partial^2 v_r}{\partial r^2} + \frac{\partial^2 v_r}{\partial z^2} + \frac{1}{r}\frac{\partial v_r}{\partial r} - \frac{v_r}{r^2} + 2M\frac{\partial c}{\partial r}\frac{\partial v_r}{\partial r} + M\frac{\partial c}{\partial z}\left(\frac{\partial v_r}{\partial z} + \frac{\partial v_z}{\partial r}\right)\right], \tag{2.6}$$

$$Re\left[\frac{\partial v_z}{\partial t} + v_r\frac{\partial v_z}{\partial r} + v_z\frac{\partial v_z}{\partial z}\right] = -\frac{\partial p}{\partial z} + e^{Mc}\left[\frac{\partial^2 v_z}{\partial r^2} + \frac{\partial^2 v_z}{\partial z^2} + \frac{1}{r}\frac{\partial v_z}{\partial r} + 2M\frac{\partial c}{\partial z}\frac{\partial v_z}{\partial z} + M\frac{\partial c}{\partial r}\left(\frac{\partial v_r}{\partial z} + \frac{\partial v_z}{\partial r}\right)\right], \tag{2.7}$$

$$Pe\left[\frac{\partial c}{\partial t} + v_r\frac{\partial c}{\partial r} + v_z\frac{\partial c}{\partial z}\right] = \left[\frac{\partial^2 c}{\partial r^2} + \frac{\partial^2 c}{\partial z^2} + \frac{1}{r}\frac{\partial c}{\partial r}\right]. \tag{2.8}$$

With the symmetry condition at the axis and no-slip at the wall, the boundary conditions for velocity and concentration read

$$\begin{aligned} r = 0 \quad &: \quad \frac{\mathrm{d}v_z}{\mathrm{d}r} = 0, \quad v_r = 0, \quad \frac{\mathrm{d}c}{\mathrm{d}r} = 0, \\ r = 1 \quad &: \quad v_z = 0, \quad v_r = 0, \quad \frac{\mathrm{d}c}{\mathrm{d}r} = 0. \end{aligned} \tag{2.9}$$

In addition to the viscosity parameter $M$, two further dimensionless parameters appear in the form of the Reynolds number $Re$ and the Péclet number $Pe$

$$Re = \frac{\rho V^* R}{\mu^*}, \qquad Pe = \frac{V^* R}{D},$$

https://doi.org/10.1017/S0022112008004242 Published online by Cambridge University Press

which indicate the ratio of convective to diffusive transport in the momentum and species conservation equations, respectively. The Péclet number and Reynolds number are related through the Schmidt number, $Sc = Pe/Re$, i.e. $Sc = \mu^*/\rho D$.

## 3. Linear stability analysis

### 3.1. *Linearization*

We decompose each governing variable ($\Phi$) into a quasi-steady parallel base state ($\bar{\Phi}$) and a perturbation ($\tilde{\Phi}$) and linearize the governing equations (2.5)–(2.8) around the parallel base state of the form (cf., Selvam *et al.* 2007)

$$\bar{c}(r) = 0.5 + 0.5 \cdot \mathrm{erf}\left(\frac{r - R_I}{\delta}\right), \tag{3.1}$$

$$\frac{\mathrm{d}\bar{p}}{\mathrm{d}z} = \mathrm{e}^{M\bar{c}}\left[\frac{\mathrm{d}^2\bar{v}_z}{\mathrm{d}r^2} + \frac{1}{r}\frac{\mathrm{d}\bar{v}_z}{\mathrm{d}r} + M\frac{\mathrm{d}\bar{v}_z}{\mathrm{d}r}\frac{\mathrm{d}\bar{c}}{\mathrm{d}r}\right]. \tag{3.2}$$

Here, $R_I$ is the interface position (core radius) and $\delta$ denotes the interface thickness. Since the spatial derivatives in the governing equations are second order, the generalized spatial eigenvalue will appear nonlinearly. Therefore, it is convenient to recast each second-order equation as a system of two first-order equations (Schmid & Henningson 2001). The discretized perturbation equations then take the matrix form

$$\partial_z\tilde{\Phi} = \boldsymbol{A}\tilde{\Phi} + \boldsymbol{B}\partial_t\tilde{\Phi}, \tag{3.3}$$

where $\tilde{\Phi} = (\tilde{c}, \partial_z\tilde{c}, \tilde{v}_r, \partial_z\tilde{v}_r, \tilde{v}_z, \tilde{p})$ is the eigenvector (see the Appendix for the entries of the matrices $\boldsymbol{A}$ and $\boldsymbol{B}$).

We perform a normal mode analysis by assuming that the perturbation is of the form

$$\tilde{\Phi}(r, z, t) = \hat{\Phi}(r)\,\mathrm{e}^{\mathrm{i}(kz - \omega t)}, \tag{3.4}$$

where $k$ is the complex spatial wavenumber and $\omega$ denotes the complex frequency. Substituting (3.4) into (3.3), we obtain a generalized eigenvalue problem satisfying the dispersion relation $D(k, \omega) = 0$. In a temporal stability framework, the perturbations are assumed to be periodic in the axial direction, i.e. for a given real wavenumber $k_r$, we seek a complex frequency $\omega = \omega_r + \mathrm{i}\,\omega_i$. In the spatial framework, the perturbations are time-periodic, i.e. for a given real $\omega_r$, we seek a complex spatial wavenumber $k = k_r + \mathrm{i}\,k_i$. In a spatio-temporal setting (as required for determining the absolute/convective nature of the instability), both the frequency and wavenumber may take on complex values. Note that both the temporal and the spatial analysis can be performed using (3.3) without changing the matrices $\boldsymbol{A}$ and $\boldsymbol{B}$. The generalized eigenvalue system (3.3) has been validated with the temporal stability results of Selvam *et al.* (2007). Further validation will be provided by means of comparison with direct numerical simulation results described below.

### 3.2. *Convective and absolute instability*

We refer the reader to Huerre & Rossi (1998) for an introduction to the basic concepts of convective and absolute instability. A detailed description with mathematical definitions and applications can also be found. Here, we briefly describe the numerical procedure to identify the transition from convective to absolute instability.

Absolute instability can be identified numerically by Briggs' method (Briggs 1964), which represents a mapping procedure involving the identification of the pinching or saddle point of the two spatial branches in the complex $k$ plane. If we define

https://doi.org/10.1017/S0022112008004242 Published online by Cambridge University Press

the corresponding frequency at the pinching point as $\omega_0$, then the flow is absolutely unstable (AU) if the imaginary part $\omega_{0,i}$ is positive. Hence, $\omega_{0,i}$ represents the absolute growth rate. Though rigorous, the practical problem with Briggs' method is that it involves the mapping of the complex $\omega$ plane to the complex $k$ plane. If we are interested only in finding the pinching point, iterative algorithms can be used (Deissler 1987). These make use of the fact that at the pinching point, the group velocity ($v_g = \partial\omega/\partial k$) is zero. By constructing a complex quadratic function for $v_g$ with $k$ as an independent parameter, it is possible to find the saddle point efficiently. Here, we follow the iterative procedure outlined in Yin *et al.* (2000) to find the absolute growth rate. For four wavenumbers $k_j$ ($j = 1, \ldots, 4$) obtained via an initial guess, the interpolating polynomial for the complex frequency $\omega$ is constructed by

$$\omega(k) = \frac{a}{3}(k - k_4)^3 + \frac{b}{2}(k - k_4)^2 + c(k - k_4) + d, \tag{3.5}$$

where $a, b, c$ and $d$ are constants that are to be determined. This is accomplished once the eigenvalue $\omega_j$ is found for each of the four $k_j$s by solving the generalized eigenvalue problem (3.3). Upon finding the constants, an improved value for $k$ is found using the saddle point criterion that $\partial\omega/\partial k = 0$

$$0 = a(k - k_4)^2 + b(k - k_4) + c. \tag{3.6}$$

Taking the root of the above quadratic equation closest to $k_4$, we form a new set of four $k_j$s and the above procedure is continued until convergence. The corresponding converged $\omega$ in the complex plane is the absolute frequency. This algorithm is computationally efficient in that, once the saddle point is found for one parameter, the values for other parameters can easily be tracked through continuation. However, whether or not such a pinching point indeed identifies an absolute mode (pinching of a $k^+$ with a $k^-$ branch, see Huerre & Rossi 1998), must formally be ascertained via Briggs' method. It has indeed been verified for selected cases, denoted in figure 2(*b*,*c*) as black squares, that the saddle point tracked in the present calculations corresponds to the pinching of a $k^+$ with a $k^-$ branch.

### 3.3. *Linear stability results*

Our objective is to find the absolute growth rate $\omega_{0,i}$ as a function of five parameters, viz. Reynolds number $Re$, Schmidt number $Sc$, viscosity ratio $M$, interface position $R_I$ and interface thickness $\delta$. We choose the reference case as $(M, Re, Sc, R_I, \delta) = (3.22, 48, 7500, 0.48, 0.02)$, which is close to the experimental parameter values of d'Olce *et al.* (submitted). A parametric study will be presented below by varying the governing parameters with respect to the reference case. Note that the interface thickness is treated as a free parameter here, since it cannot be reliably measured in experiments. However, it is reported in part 1 that the interface thickness in the experimental setting was less than the measurement resolution of 0.03.

Figure 2(*a*) shows the contour maps of constant absolute growth rate ($\omega_{0,i} = $ const.) in the ($Re$, $R_I$)-plane with all other parametes retained from the reference case. Since a positive growth rate denotes absolute instability, the marginal stability curve of $\omega_{0,i} = 0$ corresponds to the CU/AU transition in the ($Re$, $R_I$)-plane. The flow is convectively unstable at all Reynolds numbers for smaller core radii ($R_I < 0.4$). As the core thickness increases, the flow becomes absolutely unstable for a range of Reynolds numbers ($\omega_{0,i} > 0$). The transition map shows an island of absolute instability in the ($Re$, $R_I$)-plane, with both narrower and wider cores being convectively unstable. When the system is absolutely unstable, there exists an interface position with

https://doi.org/10.1017/S0022112008004242 Published online by Cambridge University Press

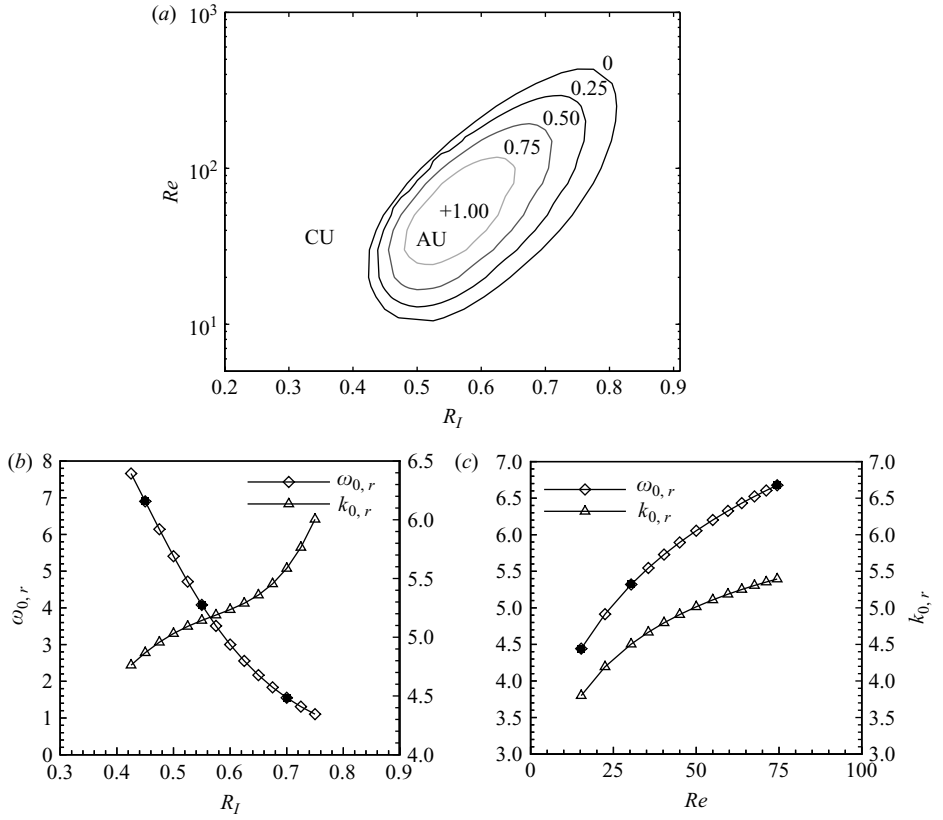



FIGURE 2. (*a*) Contour maps of constant absolute growth rate $\omega_{0,i}$ in $Re$–$R_I$ plane. Each contour is plotted as a fraction of the maximum growth rate in the $Re$–$R_I$ plane. The neutral curve, $\omega_{0,i}=0$ marks the transition from CU to AU. (*b*) Absolute real frequency $\omega_{0,r}$ and absolute wavenumber $k_{0,r}$ as functions of $R_I$ at $Re=48$. (*c*) The same quantities as functions of $Re$ at $R_I=0.48$. The other parameters are $(M, Sc, \delta)=(3.22, 7500, 0.02)$. In (*b*) and (*c*), the black squares denote the selected points that have been verified by the application of Briggs' method to ascertain that the saddle point found in the complex $k$-plane indeed corresponds to the pinching of a $k^+$-branch with a $k^-$-branch.

maximum absolute growth rate for each Reynolds number. Along with the absolute real frequency ($\omega_{0,r}$), figure 2(*b*) shows the absolute wavenumber ($k_{0,r}$) as a function of $R_I$ at fixed $Re=48$. While the absolute frequency decreases with the interface position at a given $Re$, the opposite is true for the wavenumber. However, for a given interface position, both the absolute real frequency and wavenumber increase with $Re$ (cf. figure 2*c*). These observations are in qualitative agreement with the experimental findings in part 1 and will be further discussed in § 5.

We remark that the observed CU/AU transition is not accompanied by a qualitative change in the eigenfunctions (not shown here). Close inspection reveals that the characteristic shape remains the same in both parameter regimes: vorticity perturbations peak very near the interface, on the side of the less viscous fluid. This is in agreement with earlier observations by Goyal & Meiburg (2004), Payr, Vanaparthy & Meiburg (2005) and Goyal & Meiburg (2006) for density-driven instabilities in variable viscosity flows in Hele–Shaw cells and pipes.

https://doi.org/10.1017/S0022112008004242 Published online by Cambridge University Press

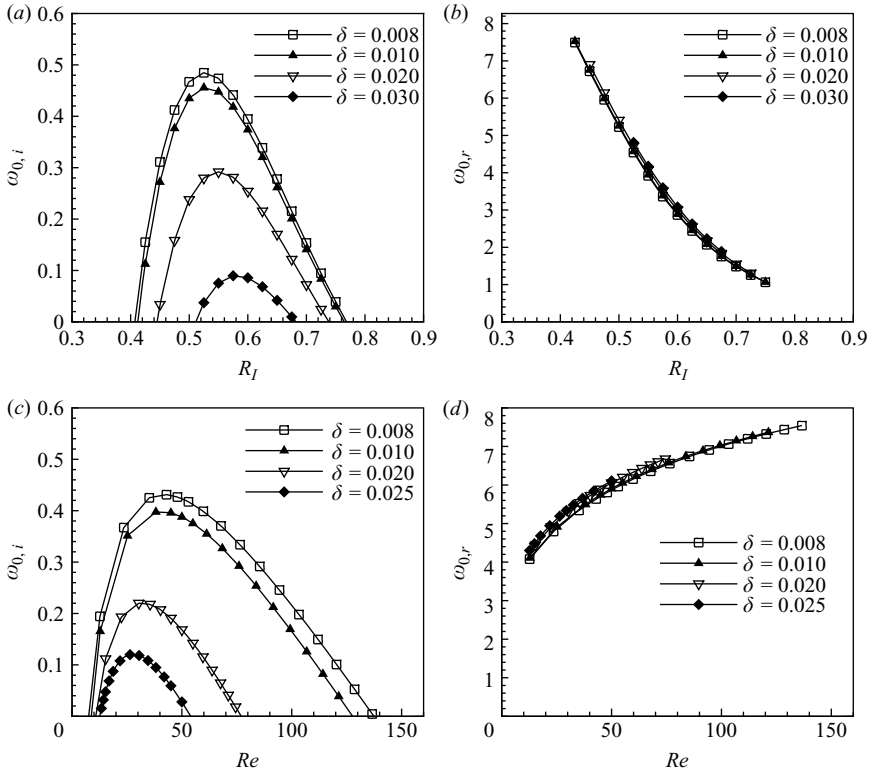



FIGURE 3. Absolute growth rate $\omega_{0,i}$ and absolute frequency $\omega_{0,r}$ for different values of $\delta$ as functions of interface position at $Re = 48$ ($a$, $b$). The same quantities as functions of Reynolds number at $R_I = 0.48$ ($c$, $d$), when $M = 3.22$ and $Sc = 7500$. Thicker interfaces uniformly stabilize the flow (complete stability is obtained for $\delta > 0.06$). The interface thickness has a negligible effect on the absolute frequency.

Figure 3 shows the absolute growth rate for varying interface thickness $\delta$. The absolute growth rate is found to decrease monotonically for increasing values of $\delta$. While the interface thickness has significant influence on the growth rate, its effect on the absolute frequency is minimal (figures 3$b$ and 3$d$). Since diffusion increases $\delta$ in the streamwise direction, the flow transitions from locally AU to locally CU, and finally to locally stable (for the parameters in figure 3, complete stability is obtained for $\delta > 0.06$). Therefore, if an absolutely unstable region exists in the spatially developing core-annular flow, this region must start at the inlet. This excludes the scenario studied in synthetic wakes (Pier & Huerre 2001) and jets (Lesshafft *et al.* 2006), where a spatially developing flow that is convectively unstable at the inlet can exhibit absolute instability further downstream.

The effect of the Schmidt number is analysed for the reference case by varying $Sc$ in the range $500$–$5 \times 10^4$ (cf. figure 4). The figure shows that the change in the maximum absolute growth rate in the parameter range considered is less than 6 %. Across this range, the Schmidt number has little influence on the stability characteristics.

Figure 5 shows the CU/AU transition in the ($Re$, $R_I$)-plane for different viscosity ratios $M$. An increase in the viscosity ratio is seen to result in a larger domain of absolute instability. For viscosity ratios $M < 2.9$, the island of absolute instability vanishes and the flow becomes convectively unstable everywhere. Thus, viscosity

https://doi.org/10.1017/S0022112008004242 Published online by Cambridge University Press

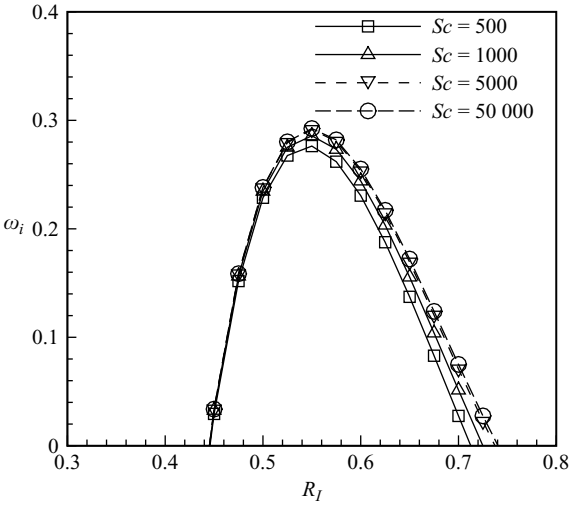



FIGURE 4. Absolute growth rate $\omega_{0,i}$ as a function of $R_I$ for $Re = 48$, $M = 3.22$, $\delta = 0.02$ and various values of $Sc$.

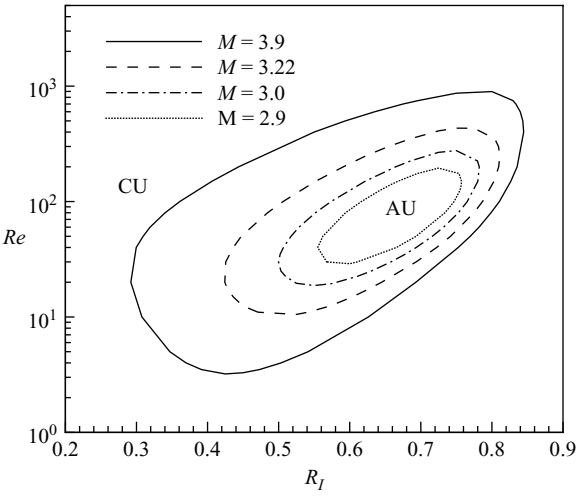



FIGURE 5. CU/AU transition map for different values of viscosity ratio $M$, when $(Sc, \delta) = (7500, 0.02)$.

ratios in excess of ($e^{2.9} = 18$) are necessary to make the flow absolutely unstable. For the sake of completeness, we carried out additional calculations for the case of less viscous fluid in the annulus ($M < 0$). Our results indicate that those systems are not absolutely unstable in the linear framework, though they can be convectively unstable. For the remainder of the paper, we will focus on positive viscosity ratios (less viscous core).

### 3.4. *Linear impulse response*

The absolute growth rate presented in the previous section characterizes the growth/decay of the perturbation at the zero group velocity ($v_g = 0$), i.e. along the $z/t = 0$ ray. However, it provides no information regarding the growth rate of the perturbation along other $z/t$ rays. We need to calculate the spatio-temporal growth rate along

https://doi.org/10.1017/S0022112008004242 Published online by Cambridge University Press

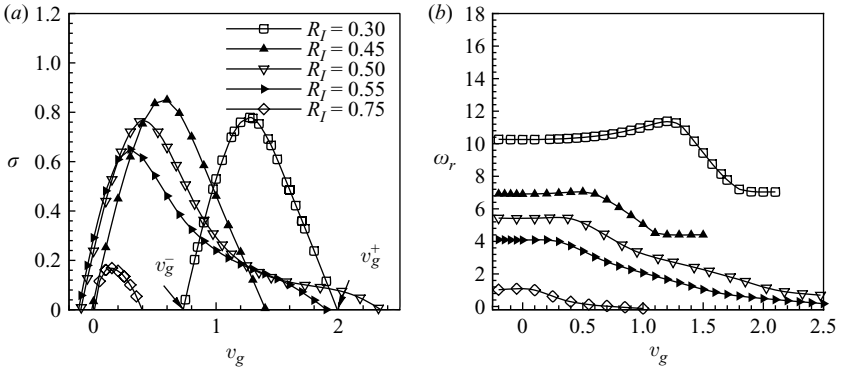



FIGURE 6. (*a*) The spatio-temporal growth rate $\sigma$, and (*b*) the real frequency $\omega_r$, as functions of the group velocity $v_g$, for $(M, Re, Sc, \delta) = (3.22, 48, 7500, 0.02)$. The trailing edge velocity $(v_g^-)$ and the leading edge velocity $(v_g^+)$ are the group velocities at which the spatio-temporal growth rate is zero on the upstream and downstream side, respectively.

each $z/t$ ray to fully characterize the evolution of the wave packet. The trailing and leading edge velocities of the wave packets, often designated by $v_g^-$ and $v_g^+$ are also of particular interest, as they determine the upstream and downstream extent of the perturbation. In this section, we calculate the linear impulse response in order to analyse the asymptotic behaviour of the system subject to initial perturbations, following the procedure outlined in Lesshafft & Huerre (2007). The growth rate along each $z/t = v_g$ ray can be obtained efficiently by calculating the absolute growth rate in a moving frame of reference ($\tilde{z} = z - v_g t$) and then transforming the results back to the laboratory frame of reference ($z$). The spatio-temporal growth rate along each $z/t$ ray is then given by $\sigma(v_g) = \tilde{\omega}_{0,i}$ and the variables in the two frames of reference are related accordingly by $\omega(v_g) = \tilde{\omega}_0 + \tilde{k}_0 v_g$ and $k(v_g) = \tilde{k}_0$ (Lesshafft & Huerre 2007). Figure 6 shows the spatio-temporal growth rate $\sigma(v_g)$, along with the real frequency $(\omega_r)$ as a function of the group velocity. The trailing and leading edge velocities of the wave packet, $v_g^-$ and $v_g^+$, are given by the group velocities at which the spatio-temporal growth rate becomes zero (shown in the figure for $R_I = 0.3$). Since the spatio-temporal growth rate at zero $v_g$ determines the absolute instability, i.e. $\sigma(0) = \omega_{0,i}$, a positive $\sigma(0)$ implies that the trailing edge velocity $v_g^-$ is negative. Hence, $v_g^-$ will be negative for AU, with the opposite being true for CU. Figure 6 shows that $v_g^-$ changes sign from a positive value if the core radius is increased from $R_I = 0.3$ to 0.45. Hence, $R_I \approx 0.45$ is the critical interface location at which the flow starts to exhibit absolute instability. For $R_I = 0.5$, the trailing edge velocity of the wave packet is negative, and any initial perturbations from the source location would propagate upstream too, invading the entire flow field. However, for a much wider core ($R_I = 0.75$), the trailing edge front velocity becomes positive again and the system is convectively unstable, as already seen in figure 2(*b*). We further discuss the front velocities in detail in § 4.3. We note that the peculiar shape at high $v_g$ found for $R_I = 0.5$ is also present at other values of $R_I$, but only at negative values of $\sigma$.

## 4. Nonlinear numerical simulation

So far, we have analysed the linear stability properties of miscible core-annular flows. in this section, direct numerical simulations (DNS) of such flows will be

https://doi.org/10.1017/S0022112008004242 Published online by Cambridge University Press

presented in order to study how nonlinear effects modify the stability characteristics, and to what extent linear predictions apply to nonlinear situations.

### 4.1. *Numerical method*

The incompressible Navier–Stokes equations (2.5)–(2.8) in primitive variables are solved using a modified fractional step method (Rai & Moin 1991; Verzicco & Orlandi 1996). It employs a three-step hybrid Runge–Kutta (RK)/Crank–Nicolson (CN) scheme for time advancement, with an explicit RK method for convective terms and an implicit CN method for viscous terms. The implicit treatment of the viscous terms is necessary to avoid the severe time-step restriction of low-Reynolds-number flows. Though the general methodology is as outlined in the above references, some differences arise due to variable viscosity. The implicit viscous terms in the axial and radial momentum equations (2.6) and (2.7) are now coupled. In our numerical implementation, decoupling is achieved via a method proposed by Li & Renardy (1999). This modification necessitates further changes in the pressure correction equation of Verzicco & Orlandi (1996). These modifications yield

$$\frac{\hat{v}_r - v_r^l}{\Delta t} = \gamma_l H_r^l + \rho_l H_r^{l-1} + \alpha_l \left[ -\frac{\partial p^l}{\partial r} + (A_{rr} + A_{rz}) \frac{\hat{v}_r + v_r^l}{2} \right], \tag{4.1}$$

$$\frac{\hat{v}_z - v_z^l}{\Delta t} = \gamma_l H_z^l + \rho_l H_z^{l-1} + \alpha_l \left[ -\frac{\partial p^l}{\partial z} + (A_{zr} + A_{zz}) \frac{\hat{v}_z + v_z^l}{2} + B_z \frac{\hat{v}_r + v_r^l}{2} \right], \tag{4.2}$$

$$\frac{v_i^{l+1} - \hat{v}_i}{\Delta t} = -\alpha_l \frac{\partial \phi^{l+1}}{\partial i}, \qquad i = r, z \tag{4.3}$$

$$\nabla^2 \phi^{l+1} = \frac{1}{\alpha_l \Delta t} \nabla \cdot \hat{\boldsymbol{v}}, \tag{4.4}$$

$$\frac{\partial p^{l+1}}{\partial r} = \frac{\partial p^l}{\partial r} + \frac{\partial \phi^{l+1}}{\partial r} - \frac{\alpha_l \Delta t}{2} (A_{rr} + A_{rz}) \frac{\partial \phi^{l+1}}{\partial r}, \tag{4.5}$$

$$\frac{\partial p^{l+1}}{\partial z} = \frac{\partial p^l}{\partial z} + \frac{\partial \phi^{l+1}}{\partial z} - \frac{\alpha_l \Delta t}{2} \left[ (A_{zr} + A_{zz}) \frac{\partial \phi^{l+1}}{\partial z} + B_z \frac{\partial \phi^{l+1}}{\partial r} \right]. \tag{4.6}$$

Here $\hat{\boldsymbol{v}} = (v_r, v_z)$ denotes the velocity field at intermediate RK substeps, $\phi$ is a scalar that is used to enforce continuity, $l = 1, 2, 3$ corresponds to the three substeps of RK method and $\gamma_l, \rho_l, \alpha_l$ are the coefficients of the time advancement scheme (Rai & Moin 1991). The other operators defined in the above notation are

$$A_{rr}(.) = \frac{2}{Re} \left[ \frac{1}{r} \frac{\partial}{\partial r} \left( r\mu \frac{\partial(.)}{\partial r} \right) - \frac{\mu(.)}{r^2} \right], \quad A_{rz}(.) = \frac{1}{Re} \left[ \frac{\partial}{\partial z} \left( \mu \frac{\partial(.)}{\partial z} \right) \right],$$

$$A_{zr}(.) = \frac{1}{Re} \left[ \frac{1}{r} \frac{\partial}{\partial r} \left( r\mu \frac{\partial(.)}{\partial r} \right) \right], \quad A_{zz}(.) = \frac{2}{Re} \left[ \frac{\partial}{\partial z} \left( \mu \frac{\partial(.)}{\partial z} \right) \right], \quad B_z(.) = \frac{1}{Re} \frac{\mu}{r} \frac{\partial(.)}{\partial z},$$

$$\nabla^2(.) = \frac{1}{r} \frac{\partial}{\partial r} \left( r \frac{\partial(.)}{\partial r} \right) + \frac{\partial^2(.)}{\partial z^2}, \qquad \nabla(.) = \frac{1}{r} \frac{\partial(r(.))}{\partial r} + \frac{\partial(.)}{\partial z},$$

$$H_r = -\left[ v_r \frac{\partial v_r}{\partial r} + v_z \frac{\partial v_r}{\partial z} \right] + \frac{1}{Re} \frac{\partial}{\partial z} \left( \mu \frac{\partial v_z}{\partial r} \right),$$

$$H_z = -\left[ v_r \frac{\partial v_z}{\partial r} + v_z \frac{\partial v_z}{\partial z} \right] + \frac{1}{Re} \frac{\partial}{\partial r} \left( \mu \frac{\partial v_r}{\partial z} \right).$$

https://doi.org/10.1017/S0022112008004242 Published online by Cambridge University Press

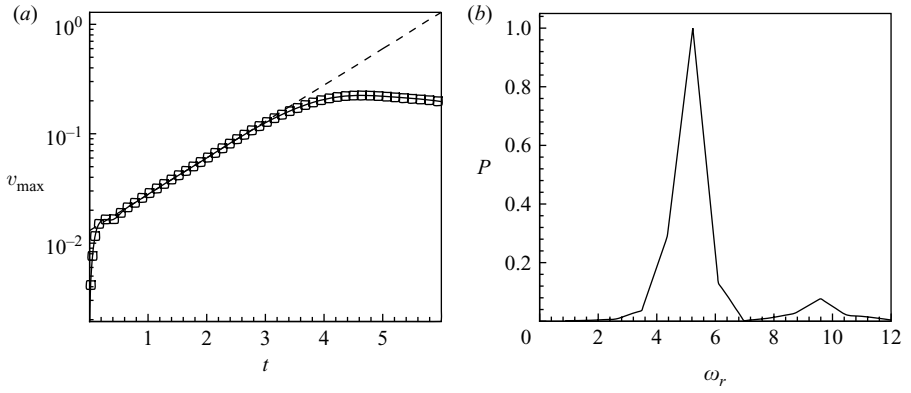



FIGURE 7. Comparison of linear stability results with nonlinear, axisymmetric simulation data for $(M, Re, Sc, R_I, \delta) = (3.22, 48, 7500, 0.5, 0.02)$. (*a*) Time evolution of the maximum radial velocity in the field (□). Dashed line is the linear fit with a slope of 0.76. (*b*) Power spectrum measured from the radial velocity at $(z, r) = (1, 0.5)$, with a maximum peak at frequency $\omega_r = 5.23$. The corresponding linear results are $(\omega_i, \omega_r) = (0.766, 5.37)$.

The momentum equations are discretized in a staggered form using second-order stencils on a non-uniform stretched mesh (Govindarajan 2004) in the $r$-direction and a uniform mesh in the $z$-direction. The direct cosine transform method (Kim & Moin 1985) is used to solve the Poisson equation (4.4). The Péclet number in the concentration equation (2.8) is $(O(10^5))$ in the present case, requiring very high accuracy for resolving the sharp gradients. The diffusion terms in the concentration equation are discretized using sixth order spectral-like resolution compact finite difference scheme (Lele 1992), while the convective terms are discretized using a Hamilton–Jacobi WENO scheme (Osher & Fedkiw 2003). For the velocity, we impose a no-slip condition at the wall and a symmetry condition at the axis. The concentration satisfies Neumann boundary conditions both at the wall and the axis, so as to enforce zero diffusive flux. The inflow and outflow as well as the initial conditions vary depending on the situation under consideration and will be mentioned when we will describe specific flows. The required grid resolution is established by means of test runs. Typically, we employ $301 \times 1025$ points in the radial and the axial directions, respectively.

### 4.2. *Validation*

We validate the DNS method with the temporal linear stability results for the case $(M, Re, Sc, R_I, \delta) = (3.22, 48, 7500, 0.5, 0.02)$. The maximum temporal growth rate for this parameter case is $\omega_i = 0.766$ and the corresponding real frequency is $\omega_r = 5.37$. In the simulation, the flow is assumed to be spatially periodic with the most amplified wavelength of the linear analysis. As initial condition, the simulation employs the base state of the linear stability analysis, superimposed with a sinusoidal interface perturbation of amplitude 0.001. Figure 7(*a*) shows the time evolution of the maximum radial velocity in the simulation. The field variable initially increases exponentially with a growth rate of 0.76 and then saturates due to nonlinear effects. The corresponding power spectrum (frequency distribution) measured from the radial velocity at $(z, r) = (1, 0.5)$ (cf. figure 7*b*), shows a peak at the frequency $\omega_r = 5.23$. These quantities lie within 3 % of the linear stability results.

https://doi.org/10.1017/S0022112008004242 Published online by Cambridge University Press

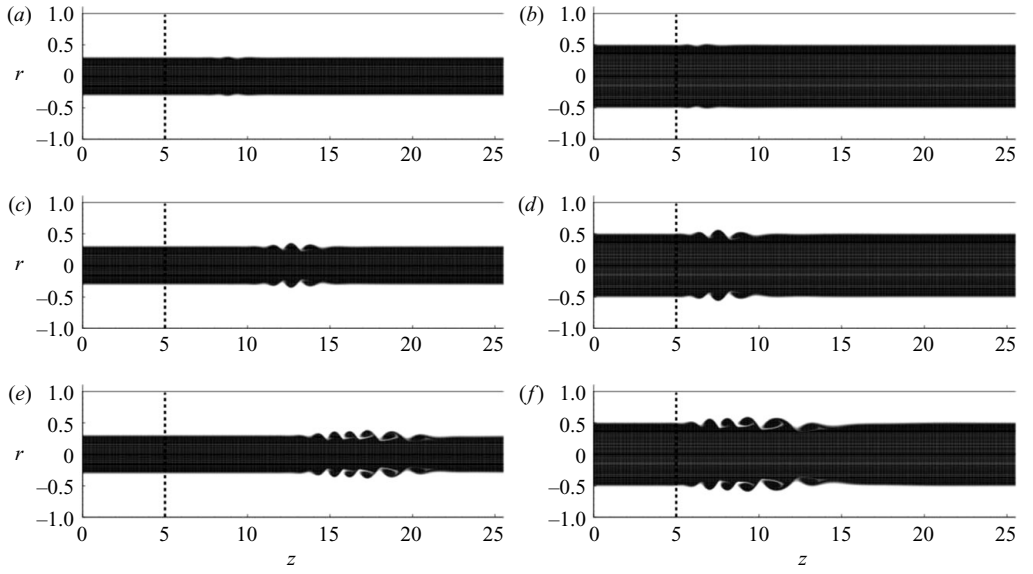



FIGURE 8. Snapshots of the nonlinear evolution of the concentration fields for core radii $R_I = 0.3$ (left) and $R_I = 0.5$ (right), at times $t = 3, 6$ and 9 (from top to bottom). The dashed line shows the location where the initial Gaussian spike is introduced. The dark fluid represents the less viscous core fluid, encapsulated by a more viscous annular fluid (white). In both cases, the initial perturbation amplifies to give rise to nonlinear rolled-up structures. However, the amplified perturbations still grow at the initial location for $R_I = 0.5$ (absolute instability), while they get advected downstream for $R_I = 0.3$ (convective instability). Note: only a portion of the $z$-axis is shown (actual domain length is 80). The other parameters are $(M, Re, Sc, \delta) = (3.22, 48, 7500, 0.02)$.

### 4.3. *Results: spatio-temporal stability of periodic flows*

In this section, we analyse nonlinear core-annular flows with periodic boundary conditions. The parallel base state used in the linear analysis (3.1) and (3.2) is prescribed as initial condition. We introduce a Gaussian spike of the following form (Delbende & Chomaz 1998) as an initial perturbation to the otherwise parallel interface:

$$R_p(z) = R_I + A_p \cdot \exp\left(-\frac{(z - z_p)^2}{\delta_p^2}\right). \tag{4.7}$$

Here, $R_I$ denotes the parallel interface position, $A_p$ the amplitude of perturbation, $z_p$ the location of the spike and $\delta_p$ the width of the Gaussian spike. In the present case, we choose these values as $(A_p, z_p, \delta_p) = (0.001, 5, 0.2)$. Note that the interface perturbation $R_p$ effectively results in a concentration perturbation through (3.1).

Figure 8 presents snapshots of the evolution of the concentration field for the two core radii $R_I = 0.3$ and 0.5. In both the cases, the flow is unstable and the initial pulse develops into nonlinear rolled-up structures. However, in the case of $R_I = 0.3$, all amplified perturbations get advected downstream. This is typical of convective instability, wherein the perturbations amplify but are swept downstream. For $R_I = 0.5$, the perturbations amplify but remain at the location of the source, demonstrating absolute instability. Recall that $R_I = 0.3$ is CU and $R_I = 0.5$ is AU from the linear analysis (figure 2*b*). These arguments can be seen more comprehensively in a spatio-temporal $(z, t)$-diagram of the perturbation enstrophy $(\eta)$ of the field, which is defined

https://doi.org/10.1017/S0022112008004242 Published online by Cambridge University Press

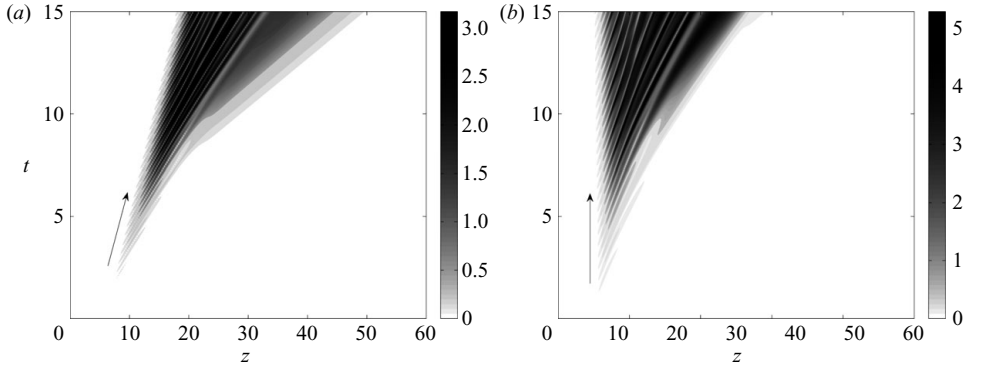



FIGURE 9. $z,t$-diagrams corresponding to the cases in figure 8. The arrows point in the direction of propagation of the trailing edge of the wave packet. ($a$) In the convective case, the trailing edge velocity is positive and the perturbations are swept downstream; $R_I = 0.3$. ($b$) When the flow is absolutely unstable, the trailing edge of the wave packet travels upstream; $R_I = 0.5$.

as

$$\eta(z,t) = \int_0^R \Omega^2(r,z,t)\, r\, \mathrm{d}r, \qquad \Omega = \frac{\partial v_r}{\partial z} - \frac{\partial v_z}{\partial r}. \tag{4.8}$$

$z,t$-diagrams of $\eta$ for the above two cases are presented in figure 9. The figure shows that the propagation direction of the trailing edge of the wave packet is positive for the convective case $R_I = 0.3$, while it is negative for the absolute case of $R_I = 0.5$. However, although $R_I = 0.5$ is AU, the upstream propagation of the wave packet is negligible, compared to the downstream propagation. This shows that the trailing edge velocity of the wave packet $v_g^-$ is quite small, in agreement with the results in figure 6. To quantify $v_g^-$, we first construct the amplitude function $A(z,t)$ encapsulating the perturbation wave packet (cf. figure 10$a$). As demonstrated in Delbende & Chomaz (1998), the amplitude function $A(z,t)$, when re-plotted in terms of the scaled variable $z/t = v_g$, can be used to retrieve the spatio-temporal growth rate given by

$$\sigma(v_g) \approx \frac{\ln\left[t_2^{1/2} A(v_g t_2, t_2) \,/\, t_1^{1/2} A(v_g t_1, t_1)\right]}{t_2 - t_1}. \tag{4.9}$$

By definition, $v_g^-$ and $v_g^+$ are the group velocities at which the spatio-temporal growth rate $\sigma(v_g)$ is zero. From (4.9), this would correspond to the group velocities at which the quantity $t^{1/2}A(v_g t, t)$ remains constant for all times. In figure 10($b$), we plot this quantity at different times in terms of the scaled variable $z/t = v_g$. In order to easily identify the linear and nonlinear regimes, we also plot the spatially averaged enstrophy $\bar{\eta}(t)$ in figure 10($c$). The perturbation amplitude initially grows exponentially demonstrating linear growth until $t \sim 6$. In the linear regime, the front velocities $v_g^-$ and $v_g^+$ are given by the crossing of the two curves ($t = 4$, 6 in figure 10$b$), as the amplitude remains constant at the intersection point. Of particular importance is $v_g^-$, since it determines the convective/absolute nature of the system. The figure shows that the linear $v_g^-$ determined from the procedure above is $-0.09$ and thus the flow is absolutely unstable. This value is to be compared to $-0.1$, obtained from the stability analysis in § 3.4. In general, we get an agreement between the two results for all other parameters within 5–10 %. Given our choice of constructing the amplitude function, this is a reasonably good agreement.

https://doi.org/10.1017/S0022112008004242 Published online by Cambridge University Press

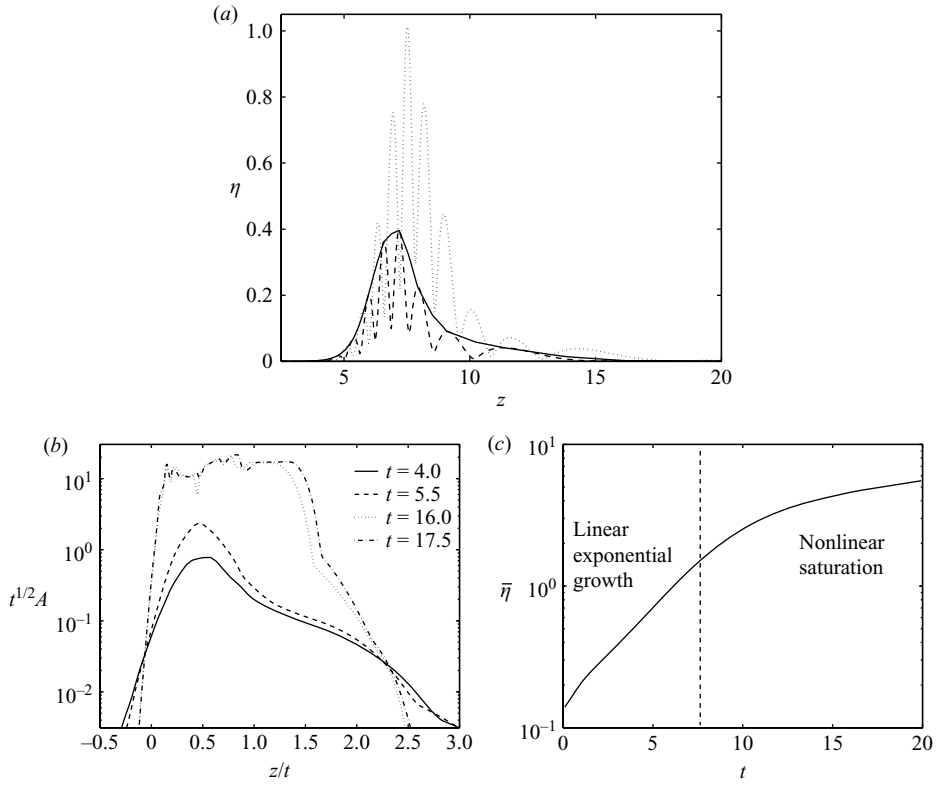



FIGURE 10. (*a*) Growth of the perturbation wave packet with time: Enstrophy $\eta$ as a function of $z$ for the core radius $R_I = 0.5$ at $t = 4$ (dashed) and $t = 5.5$ (dotted). The solid line shows the amplitude function $A(z, t)$, constructed by the piecewise cubic interpolation of the points joining the maxima of the wave packet lobes. (*b*) Scaled amplitude function in terms of $z/t = v_g$. The front velocities are given by the crossing point of the curves (see text for details). (*c*) Spatially averaged enstrophy $\bar{\eta}(t)$ ($(1/L_z)\int_0^{L_z} \eta \, \mathrm{d}z$), demonstrating the initial linear exponential growth until $t \sim 6$, followed by nonlinear saturation.

At this juncture, the natural question arises as to what the upstream front velocity is when the flow is in the nonlinear regime. Two theories have been proposed in the past. One is the 'pushed front', in which the nonlinear front moves faster than the linear front (van Saarloos 1989), while the other one is the 'pulled front', in which the nonlinear wave packet moves with the linear front velocity (Delbende & Chomaz 1998). Figure 10(*b*) shows that in the nonlinear regime ($t = 16, 17.5$), the wave packet saturates in amplitude. However, the crossing of the curves takes place at the same point as the linear front velocity $v_g^-$ before, demonstrating a 'pulled front'. As noted by Chomaz (2003), instabilities in fluid mechanics mainly fall into this category, including wake flows, Taylor–Couette instability (Büchel *et al.* 1996) and Rayleigh–Bénard instability (Müller *et al.* 1992).

### 4.4. *Nonperiodic simulations: nonlinear global modes*

We now relax the assumption of spatial periodicity and proceed to analyse nonlinear core-annular flows with a fixed upstream boundary (sketched in figure 11*a*), in configurations similar to the experiments of part 1. A direct comparison between these simulations and experimental results is attempted in § 5.

https://doi.org/10.1017/S0022112008004242 Published online by Cambridge University Press

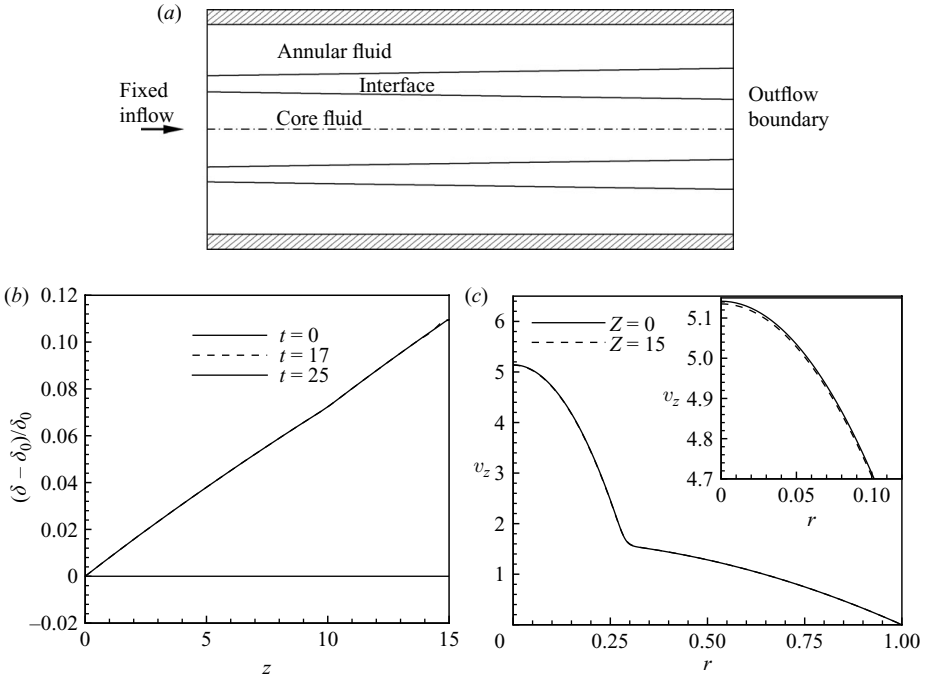



FIGURE 11. (*a*) Schematic of the non-periodic flow domain with a prescribed inlet condition. The diffused interface thickness between the core fluid and the annular fluid is drawn out of proportion for illustration. (*b*) Actual streamwise variation of the interface thickness from the simulation, relative to the inlet thickness $\delta_0 = 0.02$. The initially parallel interface at $t = 0$ relaxes to a non-parallel steady state for $t > 17$. (*c*) At $t = 25$, the axial velocity ($v_z$) profile at both the inlet ($z = 0$) and the outlet ($z = 15$). The change in the centreline velocity is within 0.15 % (figure inset showing the minor change). The other parameters are $(M, Re, Sc, R_I) = (3.22, 48, 7500, 0.3)$.

As spurious reflections from the downstream numerical boundary may lead to unwanted forcing in the interior of the domain (see Buell & Huerre 1988), a clean numerical treatment of the outflow boundary is essential for the simulation of intrinsic flow dynamics. We use a convective outflow condition, as described in Ruith, Chen & Meiburg (2004). In the present simulations, the numerical outflow is placed at a downstream location of 15 times the tube radius. Tests with various domain lengths have confirmed that this boundary treatment does not influence the interior flow behaviour. All simulations are initialized with the same parallel base states as used in the periodic configurations described in § 4.3. At the inlet, these profiles are fixed for all times as Dirichlet conditions.

In the inital stage of the simulation, the system will relax to a non-parallel base state under the influence of diffusion. In order to estimate typical rates of streamwise base flow variations, a convectively unstable configuration is run without external forcing: as expected, the flow is found to settle into a steady non-parallel state. Figure 11(*b*, *c*) display the observed variations in the interface thickness and in the flow velocity profile. Across the whole domain, the interface thickness varies by 11 %, which causes a decay of the centreline velocity of less than 0.15 %. The non-parallelism of the base flow due to diffusion may therefore be considered weak.

https://doi.org/10.1017/S0022112008004242 Published online by Cambridge University Press

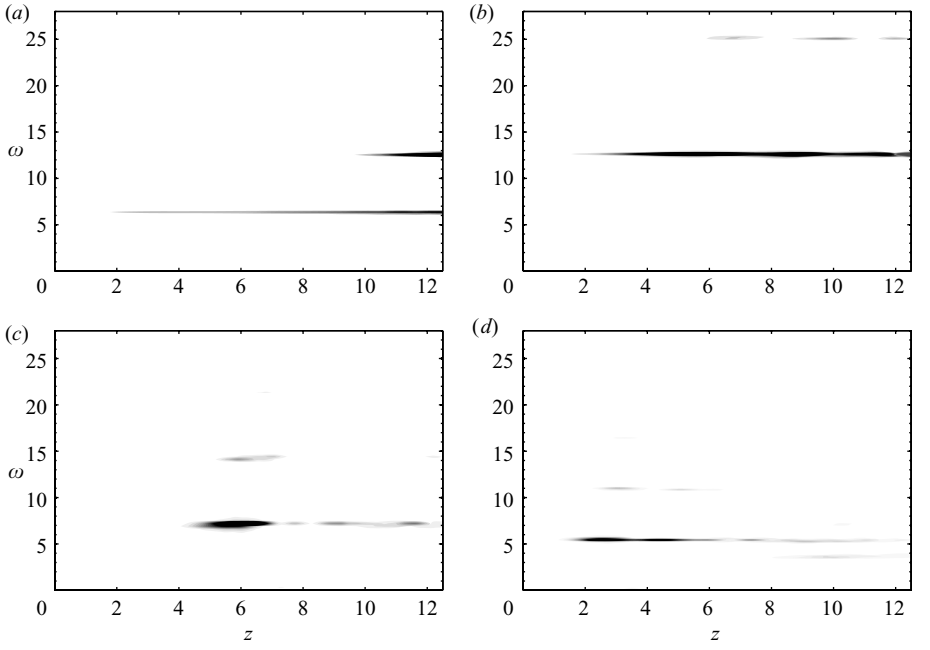



FIGURE 12. Contour plot of the power spectra in the z–$\omega$ plane, when the inlet interface position is perturbed with a forcing frequency $\omega_f$ of amplitude $10^{-3}$: (*a*) $R_I = 0.35$, $\omega_f = 6.28\ (= 2\pi)$; (*b*) $R_I = 0.35$, $\omega_f = 12.57\ (= 4\pi)$; (*c*) $R_I = 0.45$, $\omega_f = 12.57\ (= 4\pi)$ and (*d*) $R_I = 0.5$, $\omega_f = 12.57\ (= 4\pi)$. The other parameters are $(M, Re, Sc, \delta) = (3.22, 48, 7500, 0.02)$.

4.4.1. *Continuous inlet forcing*

Many systems exhibiting absolute instability (e.g. bluff body wakes) are known to sustain intrinsic oscillations, and to be insensitive to low levels of external noise. Such a spontaneous bifurcation from a steady state to a state of self-excited periodic oscillations defines a globally unstable flow situation. In contrast, convectively unstable systems respond to external noise, thus acting as noise ampifiers (Huerre & Monkewitz 1990). In order to characterize the global stability of the present core-annular flow configurations, the flow response to external forcing will be investigated first. Such forcing is provided in the simulations by prescribing sinusoidal perturbations of the inlet interface position at a single frequency $\omega_f$, with a small amplitude of $10^{-3}$. The flow is allowed to develop over a sufficiently long time, until all transient oscillations have left the computational domain. The asymptotic response to forcing is then measured as a function of $z$: at each streamwise station $z$ and at each time step, we evaluate $\int_0^1 v_r\, r\, \mathrm{d}r$. The power spectrum at each $z$ is then obtained via FFT of the temporal signal.

Contour plots of such power spectra for three-flow configurations are presented in figure 12. According to the linear stability analysis presented in § 3.3, a base flow with $R_I = 0.35$ (figure 12*a*, *b*) is convectively unstable everywhere, whereas flows with $R_I = 0.45$ and 0.5 (figure 12*c*, *d*) exhibit absolute instability near the inlet. The responses to forcing in CU and AU settings are seen to be fundamentally distinct: in the convectively unstable case, perturbations at the forcing frequency and its harmonics are amplified in the streamwise direction until nonlinear saturation occurs. In the absolutely unstable cases, in contrast, the flow oscillations synchronize

https://doi.org/10.1017/S0022112008004242 Published online by Cambridge University Press

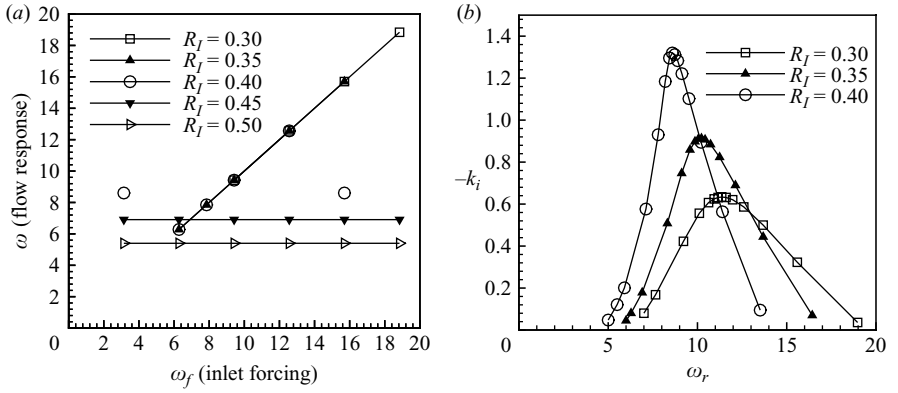



FIGURE 13. (*a*) Frequency response ($\omega$) of the system for various core radii and several values of the forcing frequency ($\omega_f$). For $R_I \leqslant 0.4$, the flow responds to low-level external forcing for a certain range of forcing frequencies (symbols connected by lines). The unconnected symbol ($\circ$) for $R_I = 0.4$ at $\omega_f = \pi, 5\pi$ represents the case where a preferred 'natural' frequency is observed near the end of the computational domain. The two-flow configurations with $R_I = 0.45$ and 0.5 always synchronize to $\omega = 6.9$ and 5.4, respectively, regardless of the forcing frequency. (*b*) Spatial growth rate ($-k_i$) calculated from the spatial linear stability analysis as function of the real frequency ($\omega_r$). The other parameters are $(M, Re, Sc, \delta) = (3.22, 48, 7500, 0.02)$.

at $\omega = 6.9$ (figure 12*c*) and $\omega = 5.4$ (figure 12*d*), whereas the forcing input is at $\omega_f = 4\pi$. Corresponding simulations have been performed for various core radii ($R_I = 0.3, 0.35, 0.4, 0.45, 0.5$) and several values of the forcing frequency. The results are summarized in figure 13(*a*), where the dominant frequency of flow oscillations near the outlet is plotted against the forcing frequency. Only the fundamental frequencies are considered here – it should be understood that harmonics are always present as soon as the oscillations reach nonlinear amplitude levels.

It is found that flows with $R_I \leqslant 0.4$ synchronize to low-level inlet forcing within a certain frequency band. For instance, a flow with $R_I = 0.35$ displays nonlinear roll-up of vortices at the imposed forcing frequency in the range $2\pi \leqslant \omega_f \leqslant 5\pi$. At forcing outside this range, two scenarios are observed: typically, only low-level amplitude fluctuations in the linear regime persist near the outlet. These cases have been omitted in figure 13(*a*). In two configurations, for $R_I = 0.4$ with $\omega_f = \pi$ and $5\pi$, noticeable oscillations at a preferred frequency $\omega = 8.6$ are observed to emerge near the end of the computational domain. Although the oscillation amplitudes do not reach nonlinear saturation within the domain, these two cases are reported in figure 13(*a*).

The two base flows with $R_I = 0.45$ and 0.5 always settle into periodic oscillations at $\omega = 6.9$ and 5.4, respectively, regardless of the forcing frequency applied at the inlet. Test calculations indicate that these flows can only be brought to synchronize to an externally imposed frequency if the interface position at the inlet is perturbed with amplitudes of the order of 1 % of the tube radius. According to the present simulation results, flows with $0.3 \leqslant R_I \leqslant 0.4$ clearly act as noise amplifiers over a band of frequencies, whereas flows with $R_I = 0.45$ and 0.5 display intrinsic oscillations. This change of behaviour between $R_I = 0.4$ and 0.45 precisely coincides with the transition from local convective to local absolute instability at the inlet, which occurs at $R_I \approx 0.425$.

For the sake of completeness, we point out that intrinsic oscillations in certain absolutely unstable flows may be suppressed and replaced by externally forced oscillation modes. The theoretical investigation of Pier (2003) provides controllability

https://doi.org/10.1017/S0022112008004242 Published online by Cambridge University Press

criteria for flows with a transition point from convective to absolute instability, which however is absent in core-annular flows. Recent experiments with low-density jets (Hallberg & Strykowski 2008) suggest that the presence of such a transition point may not be a necessary condition for controllability. An absolutely unstable flow may then respond to forcing at sufficiently high amplitudes, just as it has been observed in the present simulations.

The noise amplification in flows with $R_I \leqslant 0.4$ may be interpreted in a classical fashion on the basis of spatial linear stability analysis. Spatial growth rates $-k_i$ are plotted as functions of real frequency $\omega_r$ in figure 13($b$) for all three convectively unstable inlet profiles. It is easily verified that the ranges of spatially amplified frequencies in figure 13($b$) for all three base flows correspond precisely to the intervals in figure 13($a$) at which synchronization at the forced frequency is observed in the simulations. Furthermore, the preferred frequency ($\omega = 8.6$) for $R_I = 0.4$ at $\omega_f = \pi$ and $5\pi$ is found to be that of the most unstable spatial mode. The selection of the intrinsic oscillation frequencies in the AU regime will be investigated in detail in the following section.

### 4.4.2. *Initial impulse perturbations*

The intrinsic oscillations of absolutely unstable miscible core-annular flows, different from the forcing frequency, suggest that they might bifurcate to nonlinear global modes (Huerre & Monkewitz 1990). The nonlinear global mode solution is defined as

$$\Phi(z, r, t) = \phi(z, r)\mathrm{e}^{-\mathrm{i}\omega_G t}. \tag{4.10}$$

Here, $\omega_G$ is the global frequency. In the case of semi-infinite flows with an upstream boundary, Couairon & Chomaz (1997 $b$) have shown, in the context of a Ginzburg–Landau model, that the global frequency ($\omega_G$) agrees with the linear absolute real frequency ($\omega_{0,r}$) at the marginal threshold of absolute instability. To extend these theoretical analyses to core-annular flows, we initialize our simulation with a parallel base state and a Gaussian spike at $z = 2$, as in § 4.3. In accordance with the theory, we fix the inlet condition at $z = 0$ for all times, i.e. with fixed interface thickness ($\delta = 0.02$), and let the flow evolve without further forcing.

Figure 14 shows the measured global frequencies from the power spectrum of radial velocity, integrated over $r$, at $z = 4$, as compared with the linear absolute frequencies from the stability analysis for two different Reynolds numbers $Re = 48$ and 200. Note that the parameters for the linear stability calculations are the same as those prescribed at the inlet of the domain for the nonlinear simulation. The nonlinear global frequencies agree with the linear absolute frequencies not only at the marginal threshold but for the whole set of parameters. Such an agreement is also reported in the case of parallel wake flows (Chomaz 2003). Chomaz further noted that in the case of weakly non-parallel wakes, the selected frequency is still the absolute frequency at the inlet, though the threshold condition is altered. Thus the linear theory is successful in predicting the global stability properties in our system. This further confirms the findings of § 4.3 that the nonlinear dynamics are dictated by linear mechanisms. As mentioned in the previous section, the wave packet in an absolutely unstable medium spreads both upstream and downstream. However, in a semi-infinite domain, the perturbation amplitude has to go to zero at the inlet because of the imposed Dirichlet boundary. As a result, the propagation of the wavefront in the upstream direction is constrained and the wavefront gets saturated at some distance from the inlet (cf. figure 15$a$). To quantify this effect, the saturation distance generally known as healing length ($H_l$) is defined (Chomaz 2003)

https://doi.org/10.1017/S0022112008004242 Published online by Cambridge University Press

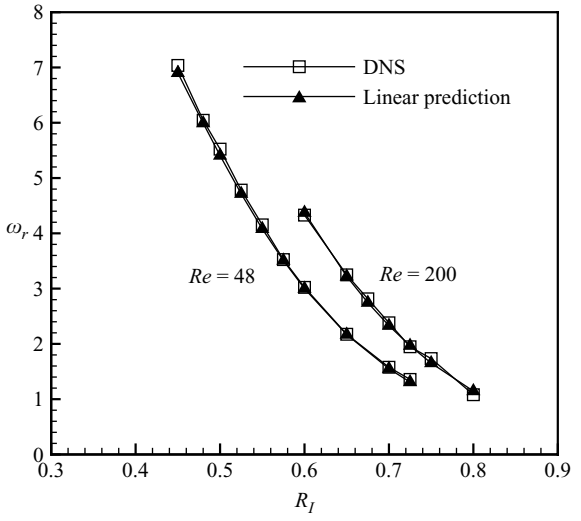



FIGURE 14. Nonlinear global mode frequency compared with the absolute linear frequency of the inlet profile, when $(M, Sc, \delta) = (3.22, 7500, 0.02)$. Nonlinear global frequencies are in close match with the absolute real frequencies. Note that for each $Re$, only the interface positions for which the flow is absolutely unstable are shown.

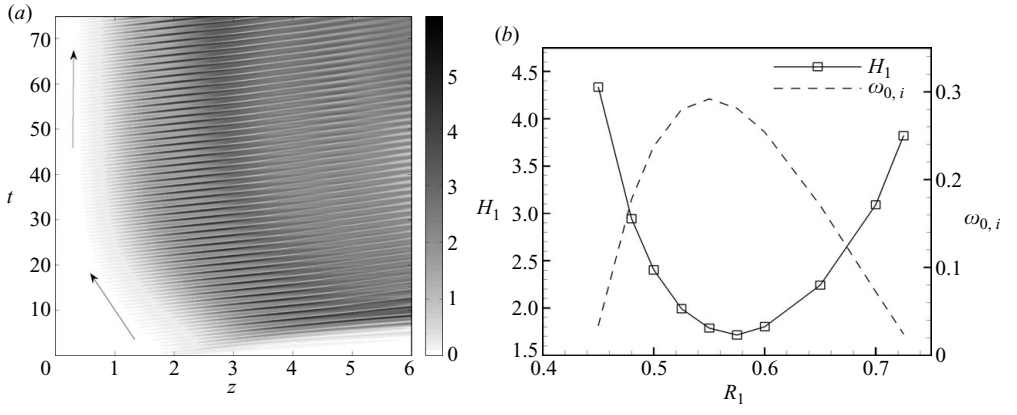



FIGURE 15. (*a*) $z, t$-diagram of the enstrophy in the case of an absolutely unstable system ($R_I = 0.55$) in a semi-infinite domain. The upstream propagation of the wavefront is constrained by the presence of the inlet boundary and the wavefront saturates at a distance, known as healing length, from the inlet. (*b*) Healing length ($H_l$) as a function of the interface position, shown along with the absolute growth rate (dashed line).

to be the distance from the inlet where the magnitude of the enstrophy becomes one. Figure 15(*b*) shows the healing length along with the absolute growth rate as a function of the interface position. When the absolute growth rate approaches zero, i.e. for a convective case, the healing length diverges. The presence of the upstream boundary does not affect the convectively unstable system (in case of no external forcing), since there is no upstream propagation of the perturbation. Hence, the saturation distance is infinite. When the flow becomes absolutely unstable, the upstream boundary is being felt by the system and the healing length decreases, with the saturation distance moving close to the inlet. We note that, unlike for parallel wake

https://doi.org/10.1017/S0022112008004242 Published online by Cambridge University Press

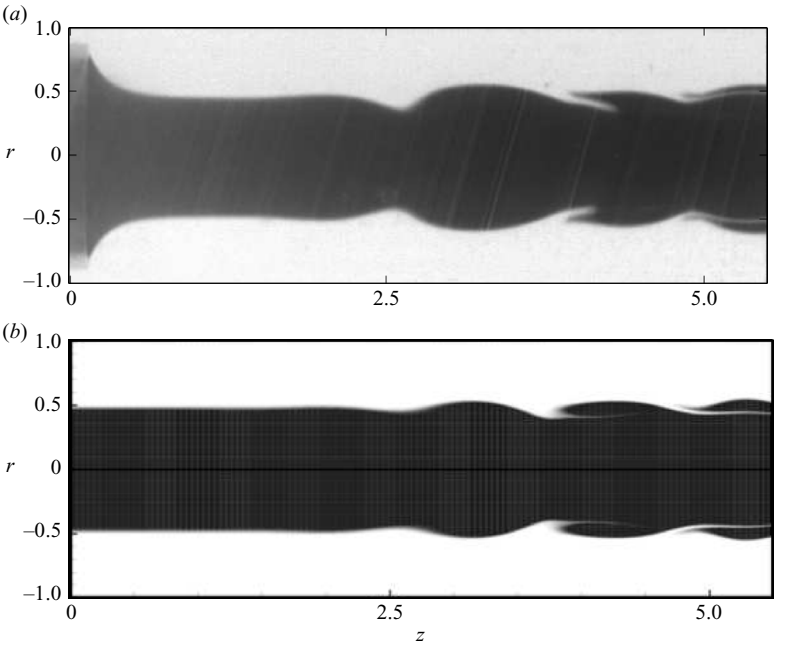



FIGURE 16. Qualitative comparison of the flow structures in (*a*) the experiment and (*b*) the DNS, for $(M, Re, Sc, R_I, \delta) = (3.22, 38, 7500, 0.48, 0.02)$.

flows, for core-annular flows the absolute growth rate and hence the healing length are non-monotonic functions of the control parameter ($R_I$), and consequently the scaling-law behaviour observed in parallel wake flows (Chomaz 2003) is not observed in this case.

## 5. Comparison with experiments

In this section, we compare the numerical results with those of the experiments in part 1. The simulations start from an initial parallel core-annular flow with a given core radius. The parallel state core radius is determined by the relative mass flow rate between the inner and the outer fluids, as described in part 1. During the entire run time of the simulation, we perturb the interface position at the inlet with random white noise of small amplitude ($10^{-3}$) to mimic the continuous feeding of randomness in the experiment. Figure 16 shows a snapshot of the flow system in the experiment and the simulation. From the figure, it can be seen that the flow structures downstream remain qualitatively the same for both the cases, demonstrating the core-annular nature of instability. Note the presence of an initial entry length in the experiment, before the flow becomes parallel. Since the simulation starts with an initial parallel core-annular flow with a prescribed core radius, the entry length is not present. Figure 17 presents the power spectra obtained from the experiment and the nonlinear simulation for two representative cases. Note that the power spectrum in the experiment was obtained from measurements of the instantaneous interface position, whereas in the present simulations it is based on the transverse velocity (see §4.4.1). When the core radius $R_I$ is 0.3, both results depict a broadband spectrum, confirming the convective instability. Since the convectively unstable system acts as noise amplifier, all of the frequencies present in the random noise at the inlet are

https://doi.org/10.1017/S0022112008004242 Published online by Cambridge University Press

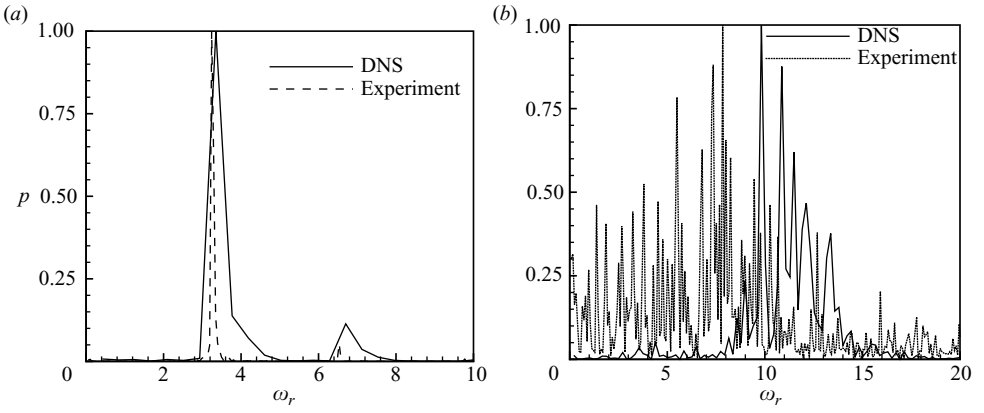



FIGURE 17. Power spectrum obtained from the experiment and the simulation at $z=4$ for two representative core radii, when $(M, Re, Sc, \delta)=(3.22, 48, 7500, 0.02)$. (*a*) When the flow is absolutely unstable ($R_I=0.57$), the spectrum peaks at single frequency, whereas for (*b*) the convective case ($R_I=0.3$), the spectrum is broadband and sensitive to external noise.

amplified. Nonetheless, it should be kept in mind that the dominant frequency will be the one with a maximum spatial growth rate. However, for $R_I=0.57$, the spectrum peaks at single frequency demonstrating absolute instability with intrinsic oscillations.

Figure 18 shows the maximum peak frequency ($\omega_r$) and the phase velocity ($c_{ph}=\omega_r/k_r$) measured from the experiment and the simulation, along with the linear stability predictions. In comparing the experimental and simulation results with the linear stability analysis, we have adopted the following procedure for the representation of the linear frequency. When the system is linearly AU, the linear frequency is unambiguously defined by the absolute frequency at the pinching point of the spatial branches. However, when the system is CU, the spatial branches do not pinch and it becomes necessary to explicitly state the frequency chosen for representation. Since the mode with the maximum spatial growth rate will dominate the flow, we have chosen the frequency corresponding to the dominant mode for comparison. Figure 18 shows that the numerical results agree with the experimental findings, i.e. for a fixed $Re=48$, both the frequency and the phase velocity exhibit a strong decrease with the increasing core radius, while for a fixed $R_I=0.48$, the frequency increases with $Re$ and the phase velocity remains almost constant.

Despite this general agreement in behaviour, one can note that both the linear analysis and the simulation somewhat overpredict the frequency. Possible reasons for the difference could be related to the initial entry length and/or experimental uncertainties at the inlet. Furthermore, in the experiments the interface position varies rapidly in the initial entry region before the flow converges to a parallel state (cf. figure 16*a*). Hence, the interface position which dictates the global mode cannot be ascertained. However, the observation that the experimental frequencies are lower than those of the numerical results (which employ the parallel core radius) can be explained from figure 14. In the range of interface positions considered in the experiment ($R_I \leqslant 0.57$), the curve for $Re=48$ in figure 14 slopes downward steeply with a 10 % reduction in frequency for every 0.02 increase in $R_I$. Since larger $R_I$-values result in lower frequencies, we can reason that the interface radius in the experiment which dictates the global mode might be larger than the parallel core radius. This, however, cannot be ascertained through the theoretical global mode analysis.

https://doi.org/10.1017/S0022112008004242 Published online by Cambridge University Press

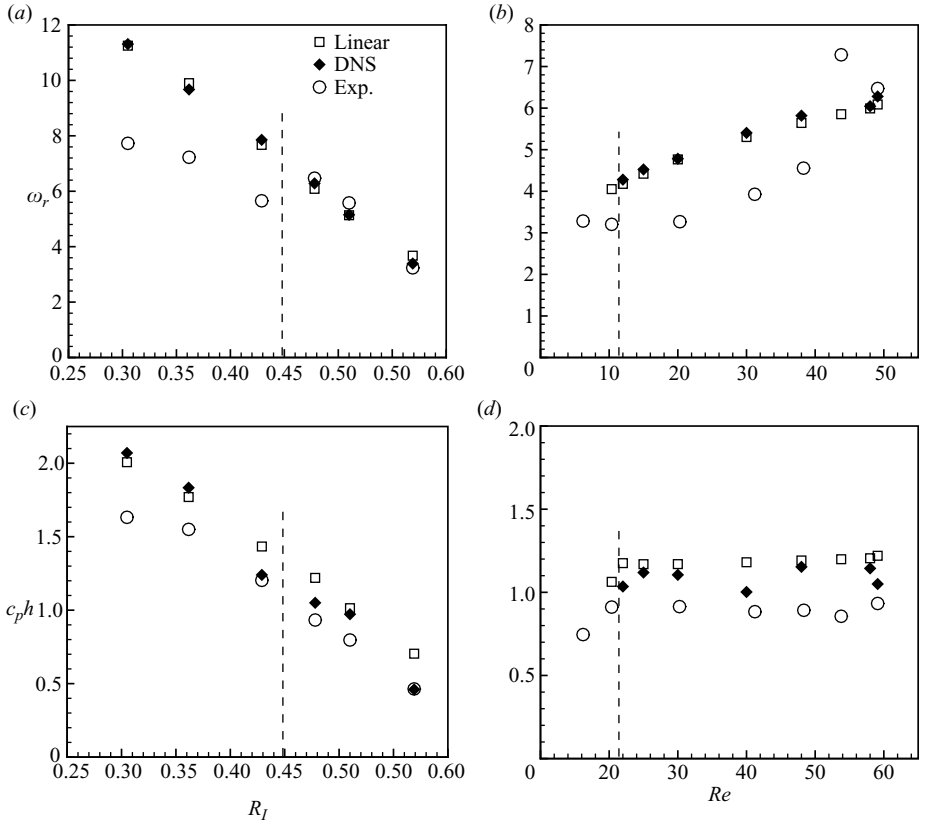



FIGURE 18. Comparison of the frequency ($\omega_r$) and the phase velocity ($c_{ph}$) obtained from the linear stability analysis, DNS and the experiment (corresponding to figure 5 in part 1). The dashed line in the above figures denotes the CU/AU transition obtained from the linear stability analysis, with the parameters to the left of the line being CU. The other parameters are $(M, Sc, \delta) = (3.22, 7500, 0.02)$.

## 6. Summary and conclusion

In the present study, we investigated numerically convective and absolute instabilities of miscible core-annular flows. When the viscosity ratio is above a critical value, miscible core-annular flows are found to be absolutely unstable. The linear stability analysis shows that a thicker interface decreases the absolute instability, while the Schmidt number is found to have little influence on the stability characteristics. It should be noted that in the stability analysis, the Schmidt number and the interface thickness are varied independently. In real flows, on the other hand, the Schmidt number has an influence on the interface thickness and hence is expected to change the stability properties.

The long-time behaviour of the edge velocities of the wave packets are characterized from the linear impulse response. When the core radius is increased, its effect on the trailing edge velocity is non-monotonic, in that it changes from positive to negative and back to positive. Thus, both narrower and wider core radii exhibit convective instability. DNS in an infinite domain with periodic boundary conditions are performed to analyse the nonlinear impulse response of the system. Similar to parallel wake flows (Chomaz 2003), the moving front is a pulled front, where the

https://doi.org/10.1017/S0022112008004242 Published online by Cambridge University Press

nonlinear front velocities match with the linear counterpart. The numerical results demonstrate that the frequency response of the intermediate core radius ($R_I = 0.5$) is insensitive to the external forcing and the oscillations are intrinsic. On the other hand, the narrower core behaves as a noise amplifier, typical of convective instability. In a semi-infinite domain with an upstream boundary, the absolutely unstable system gives rise to self-sustained oscillations with a global frequency. The observed global frequency matches with the linear absolute frequency for the parameters prescribed at the upstream boundary. This is in accordance with the theoretical predictions of Couairon & Chomaz (1997 *b*). The numerical convective/absolute characteristics of miscible core-annular flow are compared with the experimental findings of d'Olce *et al.* (submitted). Both the numerical results and the experiments show a broadband spectrum for narrower core and a sharp single frequency peak for the intermediate core. The DNS results show good agreement with predictions obtained on the basis of nonlinear global theory. Synchronized oscillations in convectively unstable flows, in the presence of random inlet forcing, may therefore be interpreted as being noise driven, whereas synchronized oscillations in absolutely unstable flows appear to be due to an intrinsic nonlinear global mode. These numerical results suggest that the synchronized behaviour observed in the experiments (part 1) is governed by the same mechanisms.

We wish to thank Professor D. Salin and Drs J. Martin, N. Rakotomalala and M. d'Olce for many fruitful discussions and for sharing their experimental results. Support from the National Science Foundation under the contract CTS-0456722 is gratefully acknowledged.

## Appendix: Matrix entries of the eigenvalue problem

Upon linearization of (2.5)–(2.8), the perturbation equations take the matrix form

$$\partial_z \tilde{\Phi} = \boldsymbol{A}\tilde{\Phi} + \boldsymbol{B}\partial_t \tilde{\Phi}, \tag{6.1}$$

where $\tilde{\Phi} = (\tilde{c}, \partial_z \tilde{c}, \tilde{v}_r, \partial_z \tilde{v}_r, \tilde{v}_z, \tilde{p})$ is the eigenvector, $\boldsymbol{A}$ is a $6 \times 6$ differential matrix with the following entries

$$\boldsymbol{A} = \begin{pmatrix} 0 & 1 & 0 & 0 & 0 & 0 \\ -D_2 & Pe\,\bar{v}_z & Pe\,\partial_r \bar{c} & 0 & 0 & 0 \\ 0 & 0 & 0 & 1 & 0 & 0 \\ 0 & -M\partial_r \bar{v}_z & A_{43} & Re\,\bar{v}_z \mathrm{e}^{-M\bar{c}} & 0 & \mathrm{e}^{-M\bar{c}} D_1 \\ 0 & 0 & -(r^{-1} + D_1) & 0 & 0 & 0 \\ A_{61} & 0 & 0 & A_{64} & \mathrm{e}^{M\bar{c}}(D_2 + M\partial_r \bar{c} D_1) & 0 \end{pmatrix}$$

and $\boldsymbol{B}$ is a $6 \times 6$ algebraic matrix with zero entries except $B_{21} = Pe$, $B_{43} = \mathrm{e}^{-M\bar{c}} Re$ and $B_{65} = -Re$. In the above notation, $D_2 = \partial_{rr} + r^{-1}\partial_r$, $D_1 = \partial_r$, $A_{43} = -D_2 + r^{-2} - 2M\partial_r \bar{c}\,\partial_r$, $A_{61} = M\,\mathrm{e}^{M\bar{c}}\left(\partial_{rr}\bar{v}_z + r^{-1}\partial_r \bar{v}_z + M\partial_r \bar{c}\,\partial_r \bar{v}_z + \partial_r \bar{v}_z D_1\right)$ and $A_{64} = \mathrm{e}^{M\bar{c}}(-r^{-1} - D_1 + M\partial_r \bar{c})$.

## REFERENCES

Bai, R., Chen, K. P. & Joseph, D. D. 1992 Lubricated pipelining: stability of core-annular flow. Part 5. Experiments and comparison with theory. *J. Fluid Mech.* **240**, 97–132.

Balasubramaniam, R., Rashidnia, N., Maxworthy, T. & Kuang, J. 2005 Instability of miscible interfaces in a cylindrical tube. *Phys. Fluids* **17**, 052103.

Boomkamp, P. A. M. & Miesen, R. H. M. 1992 Nonaxisymmetric waves in core-annular flow with a small viscosity ratio. *Phys. Fluids* **240**, 97.

https://doi.org/10.1017/S0022112008004242 Published online by Cambridge University Press

Briggs, R. J. 1964 *Electron-Stream Interaction with Plasmas*. MIT-Press.

Büchel, P., Lücke, M., Roth, D. & Schmitz, R. 1996 Pattern selection in the absolutely unstable regime as a nonlinear eigenvalue problem: Taylor vortices in axial flow. *Phys. Rev.* E **53** (5), 4764.

Buell, J. C. & Huerre, P. 1988 Onflow/outflow boundary conditions and global dynamics of spatial mixing layers. Rep. CTR-S88. Center for Turbulence Research, Stanford University pp. 19–27.

Chen, C.-Y. & Meiburg, E. 1996 Miscible displacement in capillary tubes. Part 2. Numerical simulations. *J. Fluid Mech.* **326**, 57.

Chen, K., Bai, R. & Joseph, D. D. 1990 Lubricated pipelining. Part 3. Stability of core-annular flow in vertical pipes. *J. Fluid Mech.* **214**, 251.

Chomaz, J. M. 2003 Fully nonlinear dynamics of parallel wakes. *J. Fluid. Mech.* **495**, 57.

Chomaz, J. M. 2005 Global instabilities in spatially developing flows: non-normality and nonlinearity. *Annu. Rev. Fluid Mech.* **37**, 357.

Chomaz, J. M., Huerre, P. & Redekopp, L. G. 1988 Bifurcations to local and global modes in spatially developing flows. *Phys. Rev. Lett.* **60** (1), 25–28.

Chomaz, J. M., Huerre, P. & Redekopp, L. G. 1991 A frequency selection criterion in spatially developing flows. *Stud. Appl. Maths* **84**, 119–144.

Couairon, A. & Chomaz, J. M. 1997*a* Absolute and convective instabilities, front velocities and global modes in nonlinear systems. *Phys.* D **108** (3), 236.

Couairon, A. & Chomaz, J. M. 1997*b* Pattern selection in the presence of a cross flow. *Phys. Rev. Lett.* **79** (14), 2666–2669.

Couairon, A. & Chomaz, J. M. 1999 Fully nonlinear global modes in slowly varying flows. *Phys. Fluids* **11** (12), 3688.

Deissler, R. J. 1987 The convective nature of instability in plane Poiseuille flow. *Phys. Fluids* **30** (8), 2303.

Delbende, I. & Chomaz, J. M. 1998 Non-linear convective/absolute instabilities in parallel two-dimensional wakes. *Phys. Fluids* **10** (11), 2724.

Govindarajan, R. 2004 Effect of miscibility on the linear instability of two-fluid channel flow. *Intl J. Multiphase Flow* **30**, 1177.

Goyal, N. & Meiburg, E. 2004 Unstable density stratification of miscible fluids in a vertical Hele--Shaw cell: influence of variable viscosity on the linear stability. *J. Fluid Mech.* **516**, 211–238.

Goyal, N. & Meiburg, E. 2006 Miscible displacements in Hele–Shaw cells: two-dimensional base states and their linear stability. *J. Fluid Mech.* **558**, 329.

Hallberg, M. P. & Strykowski, P. J. 2008 Open-loop control of fully nonlinear self-excited oscillations. *Phys. Fluids* **20**, 041703.

Hickox, C. E. 1971 Instability due to viscosity and density stratification in axisymmetric pipe flow. *Phys. Fluids* **14**, 251.

Hu, H. H. & Joseph, D. D. 1989 Lubricated pipelining: stability of core-annular flow. Part 2. *J. Fluid Mech.* **205**, 359.

Hu, H. H., Lundgren, T. S. & Joseph, D. D. 1990 Stability of core-annular flow with a small viscosity ratio. *Phys. Fluids* A **2** (11), 1945.

Hu, H. H. & Patankar, N. 1995 Non-axisymmetric instability of core-annular flow. *J. Fluid Mech.* **290**, 213.

Huerre, P. & Monkewitz, P. A. 1990 Local and global instabilities in spatially developing flows. *Annu. Rev. Fluid Mech.* **22**, 473.

Huerre, P. & Rossi, M. 1998 *Hydrodynamics and Nonlinear Instabilities,* Chapter 2. Cambridge University Press.

Joseph, D. D., Bai, R., Chen, K. P. & Renardy, Y. Y. 1997 Core-annular flows. *Annu. Rev. Fluid Mech.* **29**, 65.

Joseph, D. D., Renardy, Y. & Renardy, M. 1984 Instability of the flow of immiscible liquids with different viscosities in a pipe. *J. Fluid Mech.* **141**, 319.

Kim, J. & Moin, P. 1985 Application of a fractional-step method to incompressible Navier–Stokes equations. *J. Comput. Phys.* **59**, 308.

Kouris, C. & Tsamopoulos, J. 2001 Dynamics of axisymmetric core-annular flow in a straight tube. I. The more viscous fluid in the core, bamboo waves. *Phys. Fluids* **13** (4), 841.

https://doi.org/10.1017/S0022112008004242 Published online by Cambridge University Press

Kouris, C. & Tsamopoulos, J. 2002 Dynamics of axisymmetric core-annular flow in a straight tube. II. The less viscous fluid in the core, saw tooth waves. *Phys. Fluids* **14** (3), 1011.

Kuang, J., Maxworthy, T. & Petitjeans, P. 2003 Miscible displacements between silicone oils in capillary tubes. *Eur. J. Mech.* **22**, 271.

Lele, S. K. 1992 Compact finite difference schemes with spectral-like resolution. *J. Comput. Phys.* **103**, 16.

Lesshafft, L. & Huerre, P. 2007 Linear impulse response in hot round jets. *Phys. Fluids* **19**, 024102.

Lesshafft, L., Huerre, P. & Sagaut, P. 2007 Frequency selection in globally unstable round jets. *Phys. Fluids* **19**, 054108.

Lesshafft, L., Huerre, P., Sagaut, P. & Terracol, M. 2006 Nonlinear global modes in hot jets. *J. fluid Mech.* **554**, 393.

Li, J. & Renardy, Y. Y. 1999 Direct simulation of unsteady axisymmetric core-annular flow with high viscosity ratio. *J. Fluid Mech.* **391**, 123.

Monkewitz, P. A., Huerre, P. & Chomaz, J. M. 1993 Global linear stability analysis of weakly non-parallel shear flows. *J. Fluid Mech. Digital Arch.* **251**, 1–20.

Müller, H. W., Lücke, M. & Kamps, M. 1992 Transversal convection patterns in horizontal shear flow. *Phys. Rev.* A **45** (6), 3714.

d'Olce, M., Martin, J., Rakotomalala, N., Salin, D. & Talon, L. 2009 Convective/absolute instability in miscible core-annular flow. Part 1. Experiments. *J. Fluid. Mech.* **618**, 305–322.

Osher, S. & Fedkiw, R. 2003 *Level Set Methods and Dynamic Implicit Surfaces*. Springer.

Panton, R. L. 1984 *Incompressible Flow*. John Wiley & Sons.

Payr, M., Vanaparthy, S. H. & Meiburg, E. 2005 Influence of variable viscosity on density-driven instabilities in capillary tubes. *J. Fluid Mech.* **525**, 333–353.

Petitjeans, P. & Maxworthy, T. 1996 Miscible displacements in capillary tubes. Part 1. Experiments. *J. Fluid Mech.* **326**, 37.

Pier, B. 2003 Open-loop control of absolutely unstable domains. *Roy. Soc. Lond. Proc. Series* A **459** (2033), 1105–1115.

Pier, B. & Huerre, P. 2001 Nonlinear self-sustained structures and fronts in spatially developing wake flows. *J. Fluid Mech.* **435**, 145.

Pier, B., Huerre, P. & Chomaz, J. M. 2001 Bifurcation to fully nonlinear synchronized structures in slowly varying media. *Phys.* D **148** (1), 49–96.

Preziosi, L., Chen, K. & Joseph, D. D. 1989 Lubricated pipelining: stability of core-annular flow. *J. Fluid Mech.* **201**, 323.

Rai, M. M. & Moin, P. 1991 Direct simulations of turbulent flow using finite-difference schemes. *J. Comput. Phys.* **96**, 15.

Ruith, M. R., Chen, P. & Meiburg, E. 2004 Development of boundary conditions for direct numerical simulations of three-dimensional vortex breakdown phenomena in semi-infinite domains. *Comput. Fluids* **33**, 1225.

van Saarloos, W. 1989 Front propagation into unstable states. II. Linear versus nonlinear marginal stability and rate of convergence. *Phys. Rev.* A **39** (12), 6367.

Schmid, P. J. & Henningson, D. S. 2001 *Stability and Transition in Shear Flows*. Springer.

Scoffoni, J., Lajeunesse, E. & Homsy, G. M. 2001 Interface instabilities during displacements of two miscible fluids in a vertical pipe. *Phys. Fluids* **13** (3), 553.

Selvam, B., Merk, S., Govindarajan, R. & Meiburg, E. 2007 Stability of miscible core-annular flow with viscosity stratification. *J. Fluid Mech.* **592**, 23.

Tan, C. T. & Homsy, G. M. 1986 Stability of miscible displacements: rectilinear flow. *Phys. Fluids* **29**, 3549.

Verzicco, R. & Orlandi, P. 1996 A finite-difference scheme for three-dimensional incompressible flows in cylindrical coordinates. *J. Comput. Phys.* **123**, 402.

Yin, X. Y., Sun, D. J., Wei, M. J. & Wu, J. Z. 2000 Absolute and convective instability character of slender viscous vortices. *Phys. Fluids* **12** (5), 1062.

https://doi.org/10.1017/S0022112008004242 Published online by Cambridge University Press